NANO LETTERS

pubs.acs.org/NanoLett Letter

Layered Ferromagnetic Structure Caused by the Proximity Effect and Interlayer Charge Transfer for $LaNiO_3/LaMnO_3$ Superlattices

Mengqin Wang, Tao Zhu, He Bai, Zhuo Yin, Hao Xu, Wenxiao Shi, Zhe Li, Jie Zheng, Yulin Gan, Yunzhong Chen, Baogen Shen, Yuansha Chen,* Qinghua Zhang,* Fengxia Hu,* and Ji-Rong Sun*

Cite This: *Nano Lett.* 2024, 24, 1122–1129 Read Online

ACCESS | Metrics & More | Article Recommendations | Supporting Information

ABSTRACT: Magnetic proximity-induced magnetism in paramagnetic $LaNiO_3$ (LNO) has spurred intensive investigations in the past decade. However, no consensus has been reached so far regarding the magnetic order in LNO layers in relevant heterostructures. This paper reports a layered ferromagnetic structure for the (111)-oriented LNO/$LaMnO_3$ (LMO) superlattices. It is found that each period of the superlattice consisted of an insulating LNO-interfacial phase (five unit cells in thickness, ∼1.1 nm), a metallic LNO-inner phase, a poorly conductive LMO-interfacial phase (three unit cells in thickness, ∼0.7 nm), and an insulating LMO-inner phase. All four of these phases are ferromagnetic, showing different magnetizations. The Mn-to-Ni interlayer charge transfer is responsible for the emergence of a layered magnetic structure, which may cause magnetic interaction across the LNO/LMO interface and double exchange within the LMO-interfacial layer. This work indicates that the proximity effect is an effective means of manipulating the magnetic state and associated properties of complex oxides.

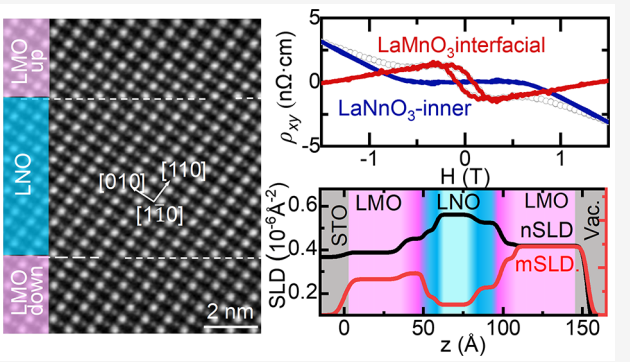

KEYWORDS: *$LaNiO_3$, $LaMnO_3$, proximity effect, charge transfer, layered ferromagnetic structure*

Due to strongly correlated electrons, transition metal oxides (TMOs) have exhibited a wide range of exotic properties, such as high-T_C superconductivity, ferromagnetism, ferroelectricity, and multiferroicity.[1−6] Among TMOs, perovskite nickelate $LaNiO_3$ (LNO), a metallic Pauli paramagnet, has attracted a great deal of research interest recently.[7] LNO usually demonstrates a rhombohedral structure, in which the Ni^{3+} ions have $3d^7$ electron configuration with a full t_{2g} shell and one electron in the degenerated e_g bands. Theoretical studies proposed that, by sandwiching an ultrathin LNO layer between insulating oxide layers such as $LaAlO_3$, one could realize a planar $d_{x^2-y^2}$ orbital order, confining the conduction to two dimensions.[8] This electronic structure is analogous to that of high-T_C superconducting cuprates,[9,10] and therefore, a tremendous amount of experimental effort has been devoted to the dependence of the transport properties of LNO on dimensionality and orbital polarization.[11−17]

Although bulk LNO lacks any magnetic order, on the contrary, LNO-based heterostructures offer new perspectives. Gibert et al. first reported an unexpected exchange-bias effect in the (111)-oriented paramagnetic/ferromagnetic (PM/FM) superlattices (SLs) that consisted of LNO and $LaMnO_3$ (LMO) sublayers.[18] Subsequent works showed that the exchange-bias effect generally existed in LNO/FM-oxide heterostructures, such as LNO/$La_{2/3}Sr_{1/3}MnO_3$ (LSMO) and LNO/$La_{2/3}Ca_{1/3}MnO_3$.[19,20] These results are interesting because the PM LNO layers have generated magnetic pining to the neighboring FM layers. This implies the development of magnetic order in the LNO layers, which is usually understood by the concept of the magnetic proximity effect.[21−27] However, there is still controversy regarding the magnetic ground state of LNO layers. On the basis of the polarization-dependent resonant X-ray reflectivity (XRR) experiments, Gibert et al. declared that the ultrathin (111)-LNO layer sandwiched between LMO layers was in an antiferromagnetic state with a (1/4, 1/4, 1/4) wavevector.[28] Later, Hoffman et al. proposed a helical spin structure for the LNO layers in the (001)-LNO/LSMO SLs, based on the polarized-neutron reflection (PNR) results.[19] Also on the basis of PNR measurement, however, Bhatt et al. claimed that the LNO-interfacial layers were FM and formed either a FM or an antiferromagnetic coupling with neighboring LSMO layers, depending on the stacking order.[29] Obviously, the controversial conclusions about the magnetic ground state of LNO have strongly impeded the understanding of such an interfacial effect and its potential applications.

Received: September 22, 2023
Revised: January 11, 2024
Accepted: January 11, 2024
Published: January 17, 2024

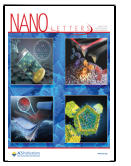

https://doi.org/10.1021/acs.nanolett.3c03658
Nano Lett. 2024, 24, 1122−1129

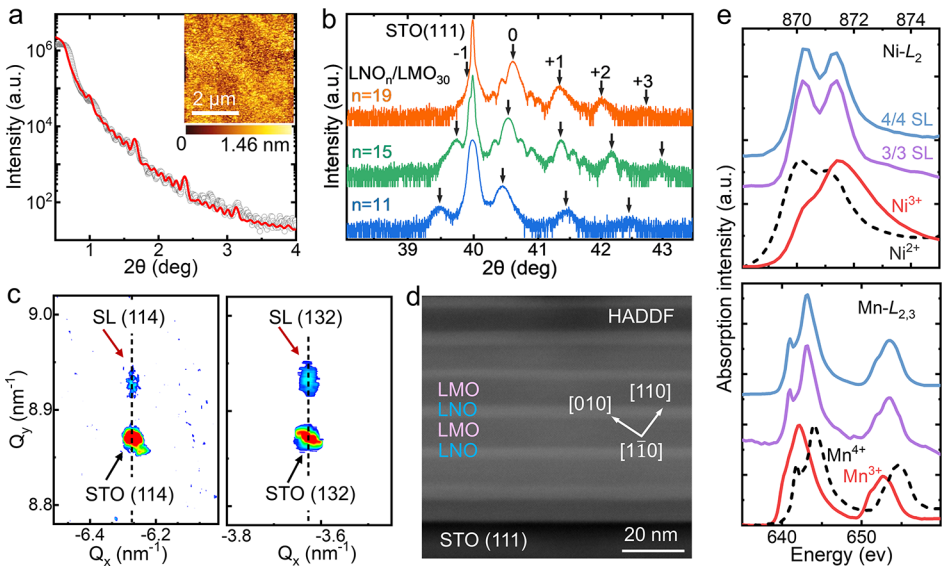

Figure 1. (a) XRR spectrum of the LNO_{15}/LMO_{30} SL (gray symbols). The thickness of each layer of the SL is obtained by curve fitting (red line). The curve fitting of the XRR confirms the well-ordered structure of the SL. The inset shows the AFM image, presenting a root-mean-squared roughness as low as ∼2.2 Å. (b) XRD spectra around the STO (111) peak of the SLs. Numbers above the curves mark satellite peaks. (c) RSM of the (114) and (132) reflections of the LNO_{15}/LMO_{30} SL. The diffraction spots of the SL (marked by red arrows) are located just above that of the substrate. (d) HAADF image of the cross section of the LNO_{15}/LMO_{30} SL, recorded along the [1$\bar{1}$0] zone axis by STEM. (e) Ni L_2 and Mn $L_{2,3}$ XAS spectra of the LNO_4/LMO_4 and LNO_3/LMO_3 SLs. For comparison, the corresponding spectra of the LNO and LMO bare films are also presented. Dashed lines are the standard Ni^{2+} L_2 edge and Mn^{4+} $L_{2,3}$ edge for NiO and MnO_2, respectively, obtained from in the literature.[34−36]

As mentioned above, the magnetic structure has already been investigated for the (111)-LNO/LMO superlattices, and an antiferromagnetic state with a (1/4, 1/4, 1/4) wavevector was reported.[28] We noticed that the investigated SLs were composed of ultrathin LNO and LMO sublayers, and the whole sublayer will be charge-doped because its thickness is comparable to the charge transfer length (approximately three to four monolayers; each sublayer has two interfaces).[30−33] What will happen to the SLs when the sublayer thickness well exceeds the length of charge transfer or the proximity effect remains an open question. In this case, the most likely process taking place in LNO or LMO will be magnetic phase separation; i.e., the magnetic state in the near interface region is different from that in the inner region of the sublayers. In this Letter, high-quality LNO/LMO SLs with remarkably thick LNO and LMO layers (11, 15, and 19 monolayers for LNO and 30 monolayers for LMO) are prepared on a (111)-oriented $SrTiO_3$ (STO) substrate and their transport and magnetic properties are systematically investigated via PNR, electron energy loss spectroscopy (EELS), X-ray absorption spectroscopy (XAS), and the Hall effect. We found layered magnetic structure that is totally different from the noncollinear antiferromagnetic structure in ultrathin LNO/LMO superlattices. Notably, layered ferromagnetic structures appear in not only LNO but also LMO. A further unusual feature is that the FM order in LNO is not limited to the interfacial layer. It extends to the inner region that is beyond the range of charge transfer, though it has a degenerated order degree now. More than that, the interfacial layer of LMO becomes conducting and exhibits a Curie temperature (250 K) much higher than that of inner LMO (180 K). Such a layered FM structure in LNO/LMO heterostructures provides a template for understanding the emergent phenomena at oxide interfaces associated with the combined effects of magnetic proximity and charge transfer.

$(LNO_n/LMO_{30})_7$ SLs were epitaxially grown on (111)-oriented STO substrates by pulsed laser deposition. Each period consists of an LMO layer of 30 u.c. and an LNO layer of n u.c., where n equals 11, 15, or 19. Notably, the interplanar distance for the (111)-LNO or LMO layer is smaller by a factor of $\sqrt{3}$ than that for the (001)-oriented layer, i.e., $d_{111} = d_{001}/\sqrt{3}$. Figure 1) shows the XRR result and surface morphology of the LNO_{15}/LMO_{30} SL, which is representative of all of the samples studied here. The Keissing fringe patterns in the XRR curve reveal the perfect periodicity of the LNO/LMO stacks. The inset AFM image also confirms the uniformity and smooth surface of the SL. The X-ray diffraction (XRD) spectra of the SLs are presented in Figure 1b. In addition to the (111) main peak, distinct satellite peaks and thickness oscillation fringes are observed, indicating the excellent quality of SLs. Because LNO has a smaller lattice constant (∼3.84 Å) compared to that of LMO (∼3.91 Å), it is natural that the (111) main peak will right shift with the increase in LNO layer thickness. Figure 1c shows the reciprocal space mapping (RSM) around the (114) and (132) reflections of the LNO_{19}/LMO_{30} SL. Vertical alignment of the diffraction spots of the SL and substrate suggests that the SL is coherently strained to the substrate along both [11$\bar{2}$] and [1$\bar{1}$0] directions. To gain knowledge of the atomic lattice structure, a high-angle annular dark-field (HAADF) image of the LNO_{15}/LMO_{30} SL is recorded by scanning transmission electron microscopy (STEM). As shown in Figure 1d, the LNO and LMO layers both grow highly epitaxially along the [111] orientation with atomically flat interfaces. All of these results reveal the high crystal quality of the samples with well-ordered SL structure.

In previous works, interlayer coupling at the LNO/LMO interface was believed to be closely related to the charge transfer between Ni and Mn ions. To determine the chemical state of Ni/Mn ions, we performed XAS analysis on the SLs as

https://doi.org/10.1021/acs.nanolett.3c03658
Nano Lett. 2024, 24, 1122−1129

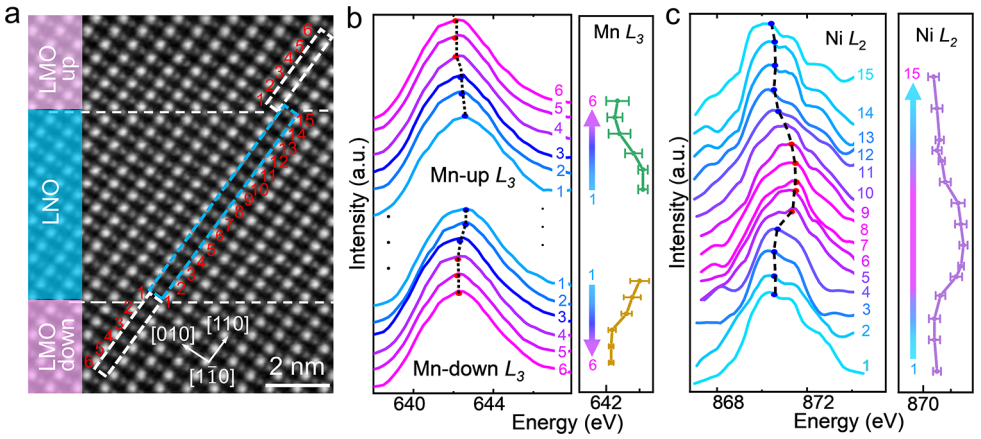

Figure 2. (a) STEM-HAADF image of LNO_{15}/LMO_{30} SLs. The dashed rectangular box indicates the region along the B-site atoms (the [110] direction), where the EELS spectra were acquired. (b and c) Layer-resolved EELS spectra of the Mn L_3 edge and Ni L_2 edge, respectively. The Ni L_3 edge is not shown here due to its overlap with the La $M_{4,5}$ edge. The averaged peak positions of the Mn L_3 edge and Ni L_2 edge are shown in the right parts of panels b and c, respectively.

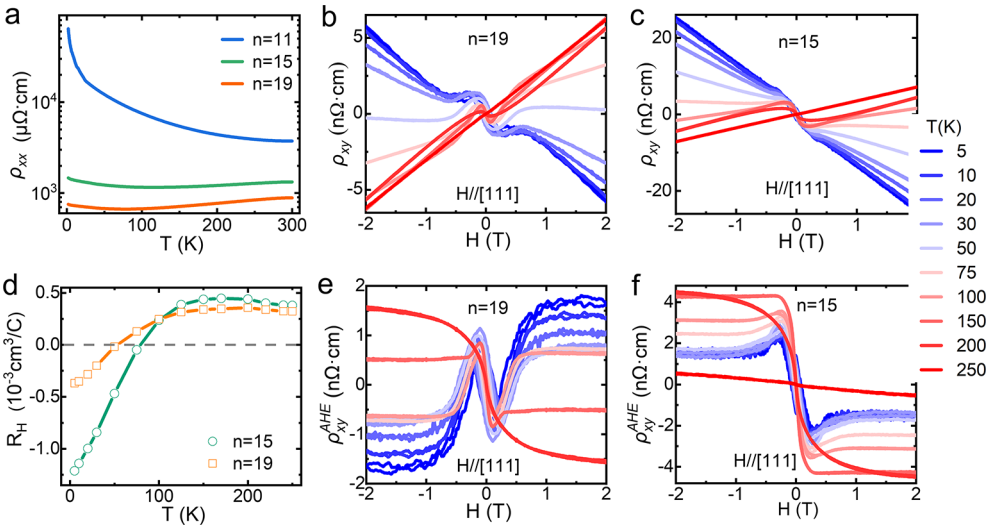

Figure 3. (a) Temperature dependence of the resistivity for the three SLs, measured from 2 to 300 K. (b) Hall resistivity as a function of magnetic field for the (b) LNO_{19}/LMO_{30} and (c) LNO_{15}/LMO_{30} SLs, measured from −2 to 2 T at temperatures ranging from 5 to 250 K. (d) Temperature dependence of ordinary Hall coefficient R_H for the LNO_{19}/LMO_{30} and LNO_{15}/LMO_{30} SLs, showing a crossover from electron type to hole type conduction. (e and f) Anomalous Hall resistivity (ρ_{xy}^{AHE}) of the LNO_{19}/LMO_{30} and LNO_{15}/LMO_{30} SLs, respectively, measured at different temperatures.

well as LNO or LMO bare films. To highlight the interfacial contributions, the LNO_3/LMO_3 and LNO_4/LMO_4 SLs, with relatively thinner period thickness, were adopted. As shown in Figure 1e, the Ni L_2-edge spectra of SLs have a double peak structure, significantly deviating from the standard Ni^{3+} spectrum of the LNO bare film but being close to the Ni^{2+} spectrum.[30,31] This suggests that the Ni ions in SLs are in a Ni^{2+}/Ni^{3+} mixed valence state close to Ni^{2+}. Correspondingly, the Mn $L_{2,3}$ edge of SLs shows a high-energy shift compared with the standard Mn^{3+} spectrum of the LMO bare film. Meanwhile, a shoulder peak emerges on the left side of the main peak, which is the typical feature of the spectrum of Mn^{4+}.[32] Therefore, Mn ions in the SL are in a valence state close to 4+. These results confirm the charge transfer from Mn to Ni ions at the LNO/LMO interface, consistent with previous reports.[30−33] A quantitative analysis shows that the valence state is 2.2+ for Ni ions and 3.8+ for Mn ions in the LNO_3/LMO_3 and LNO_4/LMO_4 SLs (Figure S1).

Notably, for the SLs with thicker LNO or LMO layers, charge transfer may mainly take place in the interface regions, resulting in interfacial layers with distinct properties. A further issue to be addressed is the thickness of each interfacial layer. To probe the range of charge transfer, spatially resolved EELS spectra were measured for the LNO_{15}/LMO_{30} SL, around the Mn $L_{2,3}$ and Ni L_2 edges (the Ni L_3 edge is not shown here due to its overlap with the La $M_{4,5}$ edge). Figure 2a is the enlarged HAADF image of one period of the SL, where the EELS line profile is conducted in the dashed box along the [110] direction. As shown in Figure 2b, the Mn L_3 edges exhibit a high-energy shift for the first three Mn−O layers near the interface; i.e., the LMO-interfacial layer is ∼3 u.c. in thickness. Correspondingly, the Ni L_2 edge exhibits a low-energy shift within five to six (or four to five) Ni−O layers near the upper (or bottom) interface. To demonstrate the layer thickness more reliably, panels b and c of Figure 2 show the statistical peak positions of the Mn L_3 edge and Ni L_2 edge layer by layer near the interface. The thicknesses of the LMO-interfacial layer

https://doi.org/10.1021/acs.nanolett.3c03658
Nano Lett. 2024, 24, 1122−1129

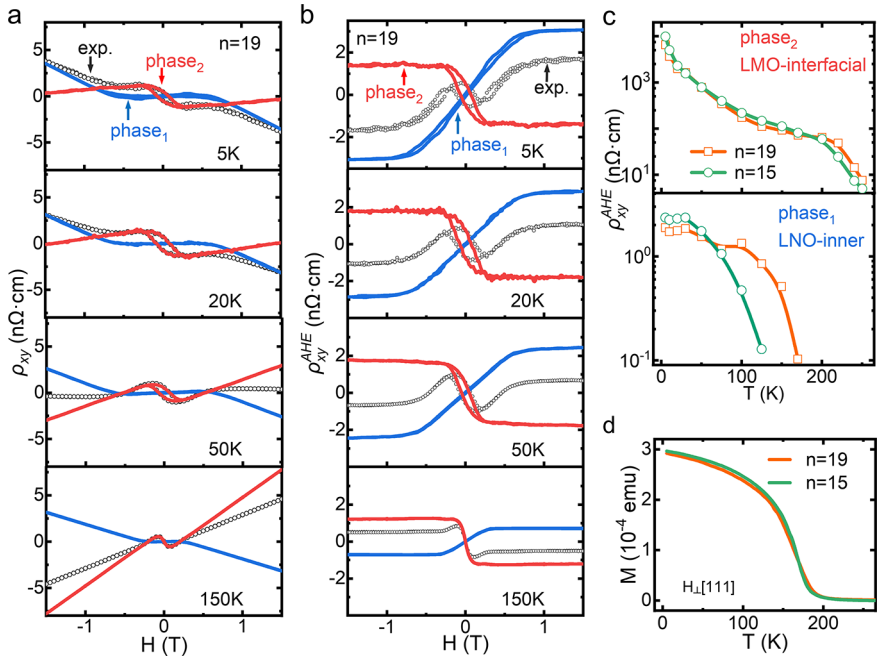

Figure 4. (a) Hall resistivity as a function of magnetic field, obtained at different temperatures for the LNO_{19}/LMO_{30} SL. Gray circles are experimental data. Blue and red lines represent the Hall resistivity of phase 1 (inner layer of LNO) and phase 2 (interfacial layer of LMO), respectively. (b) Corresponding anomalous Hall resistivity. (c) Saturation anomalous Hall resistivity (ρ_{xy}^{AHE}) as a function of temperature for the LNO_{19}/LMO_{30} and LNO_{15}/LMO_{30} SLs. The top and bottom panels show the data from the interfacial layer of LMO and the inner layer of LNO, respectively. (d) Magnetic moment as a function of temperature for the SL samples, measured with an applied field of 0.05 T.

and LNO-interfacial layer are ∼3 and ∼5 u.c., respectively. The ∼0.4 eV high-energy shift of the Mn L_3 edge suggests an ∼0.4 charge/Mn doping to the interfacial layer of LMO.

To further explore the effect of interlayer charge transfer, the transport properties of SLs are investigated. Figure 3a illustrates the temperature dependence of longitudinal resistivity ρ_{xx} for the LNO_n/LMO_{30} (n = 11, 15, and 19) SLs. LNO_{19}/LMO_{30} and LNO_{15}/LMO_{30} SLs exhibit metallic behavior in the temperature range from 70 to 300 K and a slight increase in resistance at low temperatures. In contrast, the LNO_{11}/LMO_{30} SL is completely semiconducting. As shown in Figure S2, the 11-u.c.-thick (111)-LNO single layer on STO is highly resistive, exhibiting a resistivity that is more than 1 order of magnitude higher than that of the LNO_{11}/LMO_{30} SL. Therefore, the transport behavior of LNO_{11}/LMO_{30} SL may be dominated by the interfacial layer of LMO, which becomes fairly conductive after the interlayer charge transfer that introduces holes into the LMO layer.[37] When the LNO layer is thick enough, the metallic LNO phase will appear in the inner regions of the LNO layer. Accordingly, the transport behavior of the SL exhibits a transition from a semiconducting to metallic behavior.

To determine the magnetic states of the SLs, we investigated the Hall effect. For a metallic ferromagnet, Hall resistivity can be described by the equation $\rho_{xy} = \rho_{xy}^{OHE} + \rho_{xy}^{AHE} = R_H H + R_S M$, where the first term represents the ordinary Hall effect (ρ_{xy}^{OHE}) that is proportional to applied magnetic field H and the second term is the anomalous Hall resistivity (ρ_{xy}^{AHE}) that is proportional to spontaneous magnetization M. The ρ_{xy}–H dependence of the metallic LNO_{19}/LMO_{30} and LNO_{15}/LMO_{30} SLs, measured from 5 to 250 K, is shown in panels b and c, respectively, of Figure 3. At first glance, the ρ_{xy}–H curves are warped and twisted in the low-field region and linearly shaped in the high-field region. The slopes of the linear parts give ordinary Hall coefficient R_H. Interestingly, the sign of R_H undergoes a negative to positive crossover as the temperature increases, suggesting a transition from electron type to hole type conduction (Figure 3d). This is a unique behavior of the SL samples, which is not observed in the LNO and LMO bare films.

By subtracting the linear ρ_{xy}^{OHE} contribution, we obtain the ρ_{xy}^{AHE} values for the two SLs. As shown in Figure 3e, the ρ_{xy}^{AHE}–H curves of the LNO_{19}/LMO_{30} SL exhibit a N-like twist in the low-field region and saturate at fields above 1 T. At low temperatures, saturation ρ_{xy}^{AHE} shows the same sign as H; i.e., anomalous Hall coefficient R_S is positive. The N-like twist varies regularly with an increase in temperature and finally disappears when the temperature exceeds 150 K. Correspondingly, R_S takes negative values. As mentioned above, the LNO-inner layer and the LMO-interfacial layer will both contribute to the electronic transport process of the SL. The complex dependence of the Hall effect on magnetic field could be a consequence of the competition of these two phases, resembling the Hall effect observed in some multilayers with two FM components.[38,39] Similar featured Hall curves are also observed in the LNO_{15}/LMO_{30} SL, the sample with thinner LNO layers. The difference is that now saturation ρ_{xy}^{AHE} shows the opposite sign as H regardless of temperature; i.e., R_S is always negative. Obviously, from LNO_{19}/LMO_{30} to LNO_{15}/LMO_{30}, the effective R_S at low temperatures undergoes a positive to negative transition. Considering that the contribution of the LMO-interfacial layer is highlighted by the decrease in the LNO layer thickness, this result suggests that R_S is negative for the LMO-interfacial layer and positive for the LNO-inner layer. Further evidence for this inference comes from the Hall data of the LNO_{11}/LMO_{30} SL, which shows the presence of only one FM phase with p type conduction (Figure

https://doi.org/10.1021/acs.nanolett.3c03658
Nano Lett. 2024, 24, 1122−1129

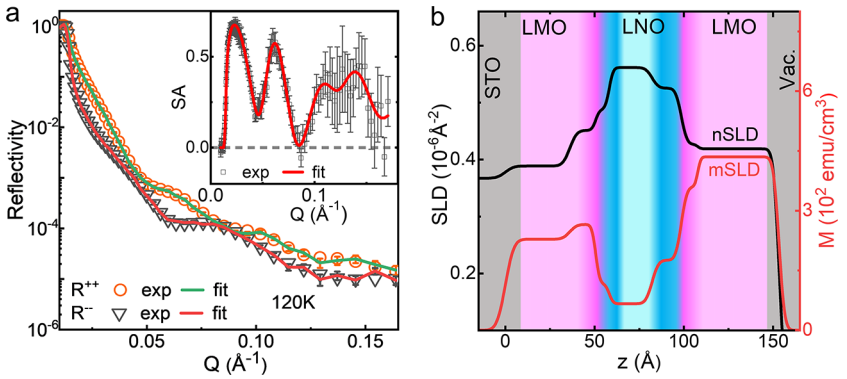

Figure 5. (a) PNR and normalized spin asymmetry data (symbols) and results of corresponding curve fitting (solid line) as a function of wave vector transfer $Q = 4\pi \sin\theta/\lambda$, obtained for the $LMO_{23}/LNO_{23}/LMO_{23}$ trilayer sample. θ is the incident angle of the neutron beam, and λ is the neutron wavelength. (b) Nuclear and magnetic scattering length density (nSLD and mSLD, respectively) profiles for the trilayer sample.

S3). As mentioned above, the transport behavior of this sample is dominated by the interfacial layer of LMO.

Combining the EELS and Hall measurement results, we propose a multilayer model for each period of the LNO/LMO SL, consisting of a LMO-inner layer, a LMO-interfacial layer, a LNO-interfacial layer, and a LNO-inner layer. According to a previous analysis, the LMO-inner layer and LNO-interfacial layer in the SLs are highly insulating. Therefore, the two FM phases seen by the Hall effect may be the metallic LNO-inner layer with Ni^{3+} ions and the semiconducting LMO-interfacial layer due to the mixing of Mn^{3+} and Mn^{4+} ions. When these two FM layers connect to each other in parallel, the effective ρ_{xx}, R_H, and ρ_{xy}^{AHE} will be[40]

$$\rho_{xx} = \frac{1}{\sigma_{xx}} = \frac{d_1 + d_2}{\sigma_1 d_1 + \sigma_2 d_2} \quad (1)$$

$$\rho_{xy}^{OHE} = R_H H = \frac{R_{H1}\sigma_1^2 d_1 + R_{H2}\sigma_2^2 d_2}{(\sigma_1 d_1 + \sigma_2 d_2)^2}(d_1 + d_2)H \quad (2)$$

$$\rho_{xy}^{AHE} = \frac{\rho_{xy_1}^{AHE}\sigma_1^2 d_1 + \rho_{xy_2}^{AHE}\sigma_2^2 d_2}{(\sigma_1 d_1 + \sigma_2 d_2)^2}(d_1 + d_2) \quad (3)$$

where the subscript 1 and 2 represent phase 1 (LNO-inner layer) and phase 2 (LMO-interfacial layer), respectively, σ is the longitudinal conductivity, and d is the layer thickness. A sketch of the layered FM structure and a detailed derivation of eqs 1−3 are available in Figure S4 and Note 1. Here, d_1 and d_2 adopt the values deduced from the depth profile analysis of SLs by STEM. When the $\rho_{xx}-T$ curves of SLs are fit to eq 1, the temperature dependence of σ_1 for the LNO-inner layer and σ_2 for the LMO-interfacial layer can be deduced. Indeed, the LNO-inner layer is metallic, whereas the LMO-interfacial layer is semiconducting (Figure S5). When parameters σ_1, σ_2, d_1, and d_2 are input into eqs 2 and 3, the $\rho_{xy}^{OHE}-H$ and $\rho_{xy}^{AHE}-H$ relations for the two FM phases are further determined. Figures 3b and 4a and Figure S6 show the results at several different temperatures for the LNO_{19}/LMO_{30} and LNO_{15}/LMO_{30} SLs. The sum of the contributions of these two phases is in good agreement with the experimental data at all temperatures. Notably, the LNO-inner layer (phase 1) shows electron type conduction and considerable AHE signals with a positive R_S sign. The latter behavior reveals the FM character of the LNO-inner phase. In contrast, the LMO-interfacial layer (phase 2) exhibits hole type conduction and is also FM with a negative R_S, which are consistent with the characteristics observed in alkali earth-doped manganite films. Deduced carrier density n as a function of T is presented in Figure S7, ranging from 10^{22} to 10^{23} cm^{-3} for the LNO-inner layer and from 10^{19} to 10^{21} cm^{-3} for the LMO-interfacial layer. With an increase in temperature, both the reversion of R_H and the evolution process of the twist-shaped $\rho_{xy}^{AHE}-H$ curves are well reproduced.

Figure 4c depicts saturation ρ_{xy}^{AHE} as a function of temperature for the LNO-inner layer and LMO-interfacial layer, where the critical temperature (T_C) of the two FM phases can be determined. For comparison, the temperature dependence of the magnetic moments ($M-T$) of the two SLs is presented in Figure 4d. As shown, the $\rho_{xy}^{AHE}-T$ curves of the LMO-interfacial layers are nearly identical for the two SLs, showing a T_C as high as ∼250 K that is higher than the value deduced from $M-T$ curves (∼190 K). This is understandable, noting that the $M-T$ curves are dominated by the inner layer of LMO, which is much thicker than the interfacial layer (24 u.c. vs 6 u.c. as indicated by the EELS spectra). One thing deserving special attention is the increase in T_C as the thickness of the LNO-inner layer increases. It is ∼125 K for the LNO_{15}/LMO_{30} SL and ∼170 K for the LNO_{19}/LMO_{30} SL. This result suggests the establishment of FM order in the inner layer of LNO; i.e., the FM order is unrestricted to the interfacial layer. As shown below by the PNR data, the middle region of the LNO layer is indeed FM, though it is ∼12 u.c. from the LNO/LMO interface. This is in sharp contrast to the $SrIrO_3$/LSMO heterostructure, for which the proximity effect-induced FM order appears only in the interfacial region.[23] A possible reason is that the mean free path of the charge carriers in metallic LNO (∼3 nm) is longer than that in semimetal $SrIrO_3$ (∼1 nm).[41−43]

The Hall measurements reveal the FM order in the LNO-inner layer. It is natural to be curious about the magnetic state of the LNO-interfacial layer, which is invisible for transport measurements. To capture the magnetic depth profile across the LNO/LMO interface, we performed PNR measurement on a $LMO_{23}/LNO_{23}/LMO_{23}$ trilayer sample. Details of PNR experiments are given in the Supporting Information. Figure 5a shows the neutron reflectivity of the trilayer, measured at 120 K with the neutron spin parallel (R^{+2}) or antiparallel (R^{-}) to the magnetic field (1.2 T). The inset plot shows the spin asymmetry defined by the equation $SA = (R^{+2} - R^{-})/(R^{+2} + R^{-})$, providing information about the depth variation of the net magnetization. A best curve fitting is obtained for the SA data

https://doi.org/10.1021/acs.nanolett.3c03658
Nano Lett. 2024, 24, 1122−1129

of PNR (SA), based on the multilayer model shown in Figure 5b. This suggests that both LNO and LMO layers are in the FM state, and the magnetic moments of all of these layers align along the same direction, implying a FM coupling between the Mn and Ni ions. The average magnetization of ∼1.0 μ_B/Ni for the LNO-interfacial layer is comparable to the value of ∼1.4 μ_B/Ni for the Ni^{2+} ions in double perovskite La_2NiMnO_6.[44] However, a low magnetization of ∼0.4 μ_B/Ni is obtained for the LNO-inner layer. This is understandable, noting the great separation between the LNO-inner layer and the LNO/LMO interface. The magnetization is ∼2.8 μ_B/Mn for the LMO-inner layer and ∼2.5 μ_B/Mn for the LMO-interfacial layer close to the right interface. This result is consistent with the picture of charge transfer, because the electron loss of the LMO-interfacial layer will result in a low magnetic moment. Moreover, we find that the magnetic order has deteriorated considerably in the left LMO layer (1.5−1.7 μ_B/Mn). This may be ascribed to the appearance of oxygen vacancies in the LMO layer adjacent to the STO substrate, as suggested by the slightly decreased nSLD of this layer. This deterioration effect usually happens to the LMO layer nearest the STO substrate. Fortunately, it does not affect the other LMO layers in the SL structure.

The XAS and EELS spectra confirm the existence of a large amount of Ni^{2+} ($t_{2g}^6e_g^2$) and Mn^{4+} ($t_{2g}^3e_g^0$) ions in the interfacial layers of LNO and LMO, respectively. According to the Goodenough−Kanamori rules, a FM superexchange interaction is expected between the Ni^{2+} and Mn^{4+} ions, resulting from the interaction of the half-filled Ni e_g orbital with a vacant Mn e_g orbital as evidenced in La_2NiMnO_6.[26,45,46] This aligns the spins of Ni ions along with the Mn ions at the interface. As a result, FM order is transferred from the LMO-interfacial layer to the LNO-interfacial layer. Due to the presence of itinerant electrons in the LNO-inner layer, the induced FM state will not be limited to the LNO-interfacial layer and extends to the metallic LNO-inner, though it is fairly far from the LNO/LMO interface.

In summary, a layered FM structure jointly caused by interlayer charge transfer and the magnetic proximity effect is detected in LNO/LMO SLs. When PM LNO is close to FM LMO, a Mn to Ni charge transfer takes place, resulting in an ∼5-u.c.-thick LNO-interfacial layer and an ∼3-u.c.-thick LMO-interfacial layer. The charge transfer also causes FM superexchange interaction between Mn^{4+} and Ni^{2+} near the interface, inducing FM order first in the LNO-interfacial layer and then in the LNO-inner layer that is far from the interface. Meanwhile, the LMO-interfacial layer becomes poorly conductive due to double exchange, showing a T_C (∼250 K) that is higher than that of the LMO-inner layer of LMO (∼190 K). The layered ferromagnetic structure in the LNO/LMO heterostrucutres provides a template for understanding the emergent phenomena at oxide interfaces associated with magnetic proximity and charge transfer effects.

EXPERIMENTAL SECTION

The details of the experimental and simulation methods are available in the Supporting Information.

ASSOCIATED CONTENT

Supporting Information

The Supporting Information is available free of charge at https://pubs.acs.org/doi/10.1021/acs.nanolett.3c03658.

Experimental details, quantitative analysis of Ni $L_{2,3}$-edge and Mn L_3-edge XAS spectra for LNO_4/LMO_4 and LNO_3/LMO_3 SLs, temperature dependence of the resistivity for the 11-u.c.-thick LNO, Hall resistivity and magnetic moment as a function of magnetic field for the LNO_{11}/LMO_{30} SL, circuit theory used to derive the resulting Hall resistivity, deduced conductivity for the LNO-inner layer and LMO-interfacial layer as a function of temperature, Hall resistivity as a function of magnetic field for the LNO_{19}/LMO_{30} and LNO_{15}/LMO_{30} SLs, and carrier density n as a function of temperature (PDF)

AUTHOR INFORMATION

Corresponding Authors

Yuansha Chen − *Beijing National Laboratory for Condensed Matter Physics and Institute of Physics, Chinese Academy of Sciences, Beijing 100190, China; School of Physical Sciences, University of Chinese Academy of Sciences, Beijing 100049, China*; Email: yschen@iphy.ac.cn

Qinghua Zhang − *Beijing National Laboratory for Condensed Matter Physics and Institute of Physics, Chinese Academy of Sciences, Beijing 100190, China; School of Physical Sciences, University of Chinese Academy of Sciences, Beijing 100049, China*; Email: zqh@iphy.ac.cn

Fengxia Hu − *Beijing National Laboratory for Condensed Matter Physics and Institute of Physics, Chinese Academy of Sciences, Beijing 100190, China; School of Physical Sciences, University of Chinese Academy of Sciences, Beijing 100049, China; Songshan Lake Materials Laboratory, Dongguan, Guangdong 523808, China*; orcid.org/0000-0003-0383-0213; Email: fxhu@iphy.ac.cn

Ji-Rong Sun − *School of Materials Science & Engineering, Taiyuan University of Science and Technology, Taiyuan 030024, China; Beijing National Laboratory for Condensed Matter Physics and Institute of Physics, Chinese Academy of Sciences, Beijing 100190, China; School of Physical Sciences, University of Chinese Academy of Sciences, Beijing 100049, China*; orcid.org/0000-0003-4531-4794; Email: jrsun@iphy.ac.cn

Authors

Mengqin Wang − *Beijing National Laboratory for Condensed Matter Physics and Institute of Physics, Chinese Academy of Sciences, Beijing 100190, China; School of Physical Sciences, University of Chinese Academy of Sciences, Beijing 100049, China*

Tao Zhu − *Beijing National Laboratory for Condensed Matter Physics and Institute of Physics, Chinese Academy of Sciences, Beijing 100190, China; Spallation Neutron Source Science Center, Dongguan 523803, China*

He Bai − *Spallation Neutron Source Science Center, Dongguan 523803, China; Institute of High Energy Physics, Chinese Academy of Sciences, Beijing 100049, China*

Zhuo Yin − *Beijing National Laboratory for Condensed Matter Physics and Institute of Physics, Chinese Academy of Sciences, Beijing 100190, China; School of Physical Sciences, University of Chinese Academy of Sciences, Beijing 100049, China*; orcid.org/0000-0002-0555-3363

Hao Xu − *Beijing National Laboratory for Condensed Matter Physics and Institute of Physics, Chinese Academy of Sciences, Beijing 100190, China; School of Physical Sciences, University of Chinese Academy of Sciences, Beijing 100049, China*

https://doi.org/10.1021/acs.nanolett.3c03658
Nano Lett. 2024, 24, 1122−1129

Wenxiao Shi − *Beijing National Laboratory for Condensed Matter Physics and Institute of Physics, Chinese Academy of Sciences, Beijing 100190, China; School of Physical Sciences, University of Chinese Academy of Sciences, Beijing 100049, China*

Zhe Li − *Beijing National Laboratory for Condensed Matter Physics and Institute of Physics, Chinese Academy of Sciences, Beijing 100190, China; School of Physical Sciences, University of Chinese Academy of Sciences, Beijing 100049, China*

Jie Zheng − *Beijing National Laboratory for Condensed Matter Physics and Institute of Physics, Chinese Academy of Sciences, Beijing 100190, China; School of Physical Sciences, University of Chinese Academy of Sciences, Beijing 100049, China*

Yulin Gan − *Beijing National Laboratory for Condensed Matter Physics and Institute of Physics, Chinese Academy of Sciences, Beijing 100190, China; School of Physical Sciences, University of Chinese Academy of Sciences, Beijing 100049, China;* orcid.org/0000-0003-0486-7026

Yunzhong Chen − *Beijing National Laboratory for Condensed Matter Physics and Institute of Physics, Chinese Academy of Sciences, Beijing 100190, China; School of Physical Sciences, University of Chinese Academy of Sciences, Beijing 100049, China;* orcid.org/0000-0001-8368-5823

Baogen Shen − *Beijing National Laboratory for Condensed Matter Physics and Institute of Physics, Chinese Academy of Sciences, Beijing 100190, China; School of Physical Sciences, University of Chinese Academy of Sciences, Beijing 100049, China; Ningbo Institute of Materials Technology & Engineering, Chinese Academy of Sciences, Ningbo, Zhejiang 315201, China;* orcid.org/0000-0003-4819-1806

Complete contact information is available at: https://pubs.acs.org/10.1021/acs.nanolett.3c03658

Notes

The authors declare no competing financial interest.

■ ACKNOWLEDGMENTS

This work has been supported by the National Key R&D Program of China (2023YFA1406003, 2022YFA1403302, 2021YFA1400300, and 2019YFA0704904), the Science Center of the National Science Foundation of China (52088101), the National Natural Science Foundation of China (11934016, 92263202, 12274443, U23A20550, and T2394472), and the Key Program of the Chinese Academy of Sciences (XDB33030200). J.-R.S. is thankful for the support of the Project for Innovative Research Team of the National Natural Science Foundation of China (11921004). The authors acknowledge Beamline BL08U1A in Shanghai Synchrotron Radiation Facility (SSRF) for the XAS characterizations, the Synergetic Extreme Condition User Facility (SECUF) for the Hall effect characterizations, and the Spallation Neutron Source Science Center for the PNR characterizations.

■ REFERENCES

(1) Takagi, H.; Hwang, H. Y. An Emergent Change of Phase for Electronics. *Science* **2010**, *327* (5973), 1601−1602.

(2) Hwang, H. Y.; Iwasa, Y.; Kawasaki, M.; Keimer, B.; Nagaosa, N.; Tokura, Y. Emergent Phenomena at Oxide Interfaces. *Nat. Mater.* **2012**, *11* (2), 103−113.

(3) Huang, Z.; Ariando; Renshaw Wang, X.; Rusydi, A.; Chen, J.; Yang, H.; Venkatesan, T. Interface Engineering and Emergent Phenomena in Oxide Heterostructures. *Adv. Mater.* **2018**, *30* (47), 1802439.

(4) Dagotto, E. Complexity in Strongly Correlated Electronic Systems. *Science* **2005**, *309* (5732), 257−262.

(5) Tokura, Y.; Nagaosa, N. Orbital Physics in Transition-Metal Oxides. *Science* **2000**, *288* (5465), 462−468.

(6) Heber, J. Thin films of oxygen-bearing compounds could have myriad practical applications, finds Joerg Heber, if a few problems can be overcome. *Nature* **2009**, *459*, 28−30.

(7) Rajeev, K. P.; Shivashankar, G. V.; Raychaudhuri, A. K. Low-Temperature Electronic Properties of a Normal Conducting Perovskite Oxide ($LaNiO_3$). *Solid State Commun.* **1991**, *79* (7), 591−595.

(8) Tao, L. L.; Tsymbal, E. Y. Two-Dimensional Type-II Dirac Fermions in a $LaAlO_3/LaNiO_3/LaAlO_3$ Quantum Well. *Phys. Rev. B* **2018**, *98* (12), 121102.

(9) Chaloupka, J.; Khaliullin, G. Orbital Order and Possible Superconductivity in $LaNiO_3/LaMO_3$ Superlattices. *Phys. Rev. Lett.* **2008**, *100* (1), 016404.

(10) Hansmann, P.; Yang, X.; Toschi, A.; Khaliullin, G.; Andersen, O. K.; Held, K. Turning a Nickelate Fermi Surface into a Cupratelike One through Heterostructuring. *Phys. Rev. Lett.* **2009**, *103* (1), 016401.

(11) Scherwitzl, R.; Gariglio, S.; Gabay, M.; Zubko, P.; Gibert, M.; Triscone, J.-M. Metal-Insulator Transition in Ultrathin $LaNiO_3$ Films. *Phys. Rev. Lett.* **2011**, *106* (24), 246403.

(12) King, P. D. C.; Wei, H. I.; Nie, Y. F.; Uchida, M.; Adamo, C.; Zhu, S.; He, X.; Božović, I.; Schlom, D. G.; Shen, K. M. Atomic-Scale Control of Competing Electronic Phases in Ultrathin $LaNiO_3$. *Nat. Nanotechnol.* **2014**, *9* (6), 443−447.

(13) Chen, B.; Gauquelin, N.; Jannis, D.; Cunha, D. M.; Halisdemir, U.; Piamonteze, C.; Lee, J. H.; Belhadi, J.; Eltes, F.; Abel, S.; Jovanović, Z.; Spreitzer, M.; Fompeyrine, J.; Verbeeck, J.; Bibes, M.; Huijben, M.; Rijnders, G.; Koster, G. Strain-Engineered Metal-to-Insulator Transition and Orbital Polarization in Nickelate Superlattices Integrated on Silicon. *Adv. Mater.* **2020**, *32* (50), 2004995.

(14) Fowlie, J.; Gibert, M.; Tieri, G.; Gloter, A.; Íñiguez, J.; Filippetti, A.; Catalano, S.; Gariglio, S.; Schober, A.; Guennou, M.; Kreisel, J.; Stéphan, O.; Triscone, J.-M. Conductivity and Local Structure of $LaNiO_3$ Thin Films. *Adv. Mater.* **2017**, *29* (18), 1605197.

(15) Kumah, D. P.; Disa, A. S.; Ngai, J. H.; Chen, H.; Malashevich, A.; Reiner, J. W.; Ismail-Beigi, S.; Walker, F. J.; Ahn, C. H. Tuning the Structure of Nickelates to Achieve Two-Dimensional Electron Conduction. *Adv. Mater.* **2014**, *26* (12), 1935−1940.

(16) Fowlie, J.; Lichtensteiger, C.; Gibert, M.; Meley, H.; Willmott, P.; Triscone, J.-M. Thickness-Dependent Perovskite Octahedral Distortions at Heterointerfaces. *Nano Lett.* **2019**, *19* (6), 4188−4194.

(17) Benckiser, E.; Haverkort, M. W.; Brück, S.; Goering, E.; Macke, S.; Frañó, A.; Yang, X.; Andersen, O. K.; Cristiani, G.; Habermeier, H.-U.; Boris, A. V.; Zegkinoglou, I.; Wochner, P.; Kim, H.-J.; Hinkov, V.; Keimer, B. Orbital Reflectometry of Oxide Heterostructures. *Nat. Mater.* **2011**, *10* (3), 189−193.

(18) Gibert, M.; Zubko, P.; Scherwitzl, R.; Íñiguez, J.; Triscone, J.-M. Exchange Bias in $LaNiO_3$-$LaMnO_3$ Superlattices. *Nat. Mater.* **2012**, *11* (3), 195−198.

(19) Hoffman, J. D.; Kirby, B. J.; Kwon, J.; Fabbris, G.; Meyers, D.; Freeland, J. W.; Martin, I.; Heinonen, O. G.; Steadman, P.; Zhou, H.; Schlepütz, C. M.; Dean, M. P. M.; Te Velthuis, S. G. E.; Zuo, J.-M.; Bhattacharya, A. Oscillatory Noncollinear Magnetism Induced by Interfacial Charge Transfer in Superlattices Composed of Metallic Oxides. *Phys. Rev. X* **2016**, *6* (4), 041038.

(20) Soltan, S.; Macke, S.; Ilse, S. E.; Pennycook, T.; Zhang, Z. L.; Christiani, G.; Benckiser, E.; Schütz, G.; Goering, E. Ferromagnetic Order Controlled by the Magnetic Interface of LaNiO3/La2/3Ca1/3MnO3 Superlattices. *Sci. Rep.* **2023**, *13* (1), 3847.

(21) Caputo, M.; Ristic, Z.; Dhaka, R. S.; Das, T.; Wang, Z.; Matt, C. E.; Plumb, N. C.; Guedes, E. B.; Jandke, J.; Naamneh, M.; Zakharova, A.; Medarde, M.; Shi, M.; Patthey, L.; Mesot, J.; Piamonteze, C.; Radović, M. Proximity-Induced Novel Ferromagnetism Accompanied

with Resolute Metallicity in $NdNiO_3$ Heterostructure. *Adv. Sci.* **2021**, *8* (19), 2101516.
(22) Skoropata, E.; Nichols, J.; Ok, J. M.; Chopdekar, R. V.; Choi, E. S.; Rastogi, A.; Sohn, C.; Gao, X.; Yoon, S.; Farmer, T.; Desautels, R. D.; Choi, Y.; Haskel, D.; Freeland, J. W.; Okamoto, S.; Brahlek, M.; Lee, H. N. Interfacial Tuning of Chiral Magnetic Interactions for Large Topological Hall Effects in $LaMnO_3/SrIrO_3$ Heterostructures. *Sci. Adv.* **2020**, *6* (27), 3902.
(23) Yoo, M.-W.; Tornos, J.; Sander, A.; Lin, L.-F.; Mohanta, N.; Peralta, A.; Sanchez-Manzano, D.; Gallego, F.; Haskel, D.; Freeland, J. W.; Keavney, D. J.; Choi, Y.; Strempfer, J.; Wang, X.; Cabero, M.; Vasili, H. B.; Valvidares, M.; Sanchez-Santolino, G.; Gonzalez-Calbet, J. M.; Rivera, A.; Leon, C.; Rosenkranz, S.; Bibes, M.; Barthelemy, A.; Anane, A.; Dagotto, E.; Okamoto, S.; Te Velthuis, S. G. E.; Santamaria, J.; Villegas, J. E. Large Intrinsic Anomalous Hall Effect in $SrIrO_3$ Induced by Magnetic Proximity Effect. *Nat. Commun.* **2021**, *12* (1), 3283.
(24) Jaiswal, A. K.; Wang, D.; Wollersen, V.; Schneider, R.; Tacon, M. L.; Fuchs, D. Direct Observation of Strong Anomalous Hall Effect and Proximity-Induced Ferromagnetic State in $SrIrO_3$. *Adv. Mater.* **2022**, *34* (14), 2109163.
(25) Anderson, P. W. Antiferromagnetism. Theory of Superexchange Interaction. *Phys. Rev.* **1950**, *79* (2), 350−356.
(26) Goodenough, J. B. Theory of the Role of Covalence in the Perovskite-Type Manganites [La, M (II)] MnO_3. *Phys. Rev.* **1955**, *100* (2), 564−573.
(27) Kanamori, J. Superexchange Interaction and Symmetry Properties of Electron Orbitals. *J. Phys. Chem. Solids* **1959**, *10* (2−3), 87−98.
(28) Gibert, M.; Viret, M.; Zubko, P.; Jaouen, N.; Tonnerre, J.-M.; Torres-Pardo, A.; Catalano, S.; Gloter, A.; Stéphan, O.; Triscone, J.-M. Interlayer Coupling through a Dimensionality-Induced Magnetic State. *Nat. Commun.* **2016**, *7* (1), 11227.
(29) Bhatt, H.; Kumar, Y.; Prajapat, C. L.; Kinane, C. J.; Caruana, A.; Langridge, S.; Basu, S.; Singh, S. Emergent Interfacial Ferromagnetism and Exchange Bias Effect in Paramagnetic/Ferromagnetic Oxide Heterostructures. *Adv. Mater. Interfaces* **2020**, *7* (21), 2001172.
(30) Piamonteze, C.; Gibert, M.; Heidler, J.; Dreiser, J.; Rusponi, S.; Brune, H.; Triscone, J.-M.; Nolting, F.; Staub, U. Interfacial Properties of LaMnO3/ LaNiO3 Superlattices Grown along (001) and (111) Orientations. *Phys. Rev. B* **2015**, *92* (1), 014426.
(31) Kitamura, M.; Horiba, K.; Kobayashi, M.; Sakai, E.; Minohara, M.; Mitsuhashi, T.; Fujimori, A.; Nagai, T.; Fujioka, H.; Kumigashira, H. Spatial Distribution of Transferred Charges across the Heterointerface between Perovskite Transition Metal Oxides $LaNiO_3$ and $LaMnO_3$. *Appl. Phys. Lett.* **2016**, *108* (11), 111603.
(32) Kitamura, M.; Kobayashi, M.; Sakai, E.; Minohara, M.; Yukawa, R.; Shiga, D.; Amemiya, K.; Nonaka, Y.; Shibata, G.; Fujimori, A.; Fujioka, H.; Horiba, K.; Kumigashira, H. Relationship between Charge Redistribution and Ferromagnetism at the Heterointerface between the Perovskite Oxides $LaNiO_3$ and $LaMnO_3$. *Phys. Rev. B* **2019**, *100* (24), 245132.
(33) Gibert, M.; Viret, M.; Torres-Pardo, A.; Piamonteze, C.; Zubko, P.; Jaouen, N.; Tonnerre, J.-M.; Mougin, A.; Fowlie, J.; Catalano, S.; Gloter, A.; Stéphan, O.; Triscone, J.-M. Interfacial Control of Magnetic Properties at $LaMnO_3/LaNiO_3$ Interfaces. *Nano Lett.* **2015**, *15* (11), 7355−7361.
(34) Cao, Y.; Liu, X.; Kareev, M.; Choudhury, D.; Middey, S.; Meyers, D.; Kim, J.-W.; Ryan, P. J.; Freeland, J. W.; Chakhalian, J. Engineered Mott Ground State in a $LaTiO_{3+\delta}/LaNiO_3$ Heterostructure. *Nat. Commun.* **2016**, *7* (1), 10418.
(35) Medarde, M.; Fontaine, A.; García-Muñoz, J. L.; Rodríguez-Carvajal, J.; De Santis, M.; Sacchi, M.; Rossi, G.; Lacorre, P. $RNiO_3$ Perovskites (R = Pr,Nd): Nickel Valence and the Metal-Insulator Transition Investigated by X-Ray-Absorption Spectroscopy. *Phys. Rev. B* **1992**, *46* (23), 14975−14984.
(36) Kim, D. H.; Lee, E.; Kim, H. W.; Kolesnik, S.; Dabrowski, B.; Kang, C.-J.; Kim, M.; Min, B. I.; Lee, H.-K.; Kim, J.-Y.; Kang, J.-S. Correlation between Mn and Ru Valence States and Magnetic Phases in $SrMn_{1-x}Ru_xO_3$. *Phys. Rev. B* **2015**, *91* (7), 075113.
(37) Ju, H. L.; Sohn, H.-C.; Krishnan, K. M. Evidence for O2p Hole-Driven Conductivity in La1-xSrxMnO3 ($0 \leq x \leq 0.7$) and La0.7Sr0.3MnOz Thin Films. *Phys. Rev. Lett.* **1997**, *79*, 3230.
(38) Kimbell, G.; Kim, C.; Wu, W.; Cuoco, M.; Robinson, J. W. A. Challenges in Identifying Chiral Spin Textures via the Topological Hall Effect. *Commun. Mater.* **2022**, *3* (1), 19.
(39) Wang, H.; Dai, Y.; Chow, G.-M.; Chen, J. Topological Hall Transport: Materials, Mechanisms and Potential Applications. *Prog. Mater. Sci.* **2022**, *130*, 100971.
(40) Petritz, R. L. Theory of an Experiment for Measuring the Mobility and Density of Carriers in the Space-Charge Region of a Semiconductor Surface. *Phys. Rev.* **1958**, *110* (6), 1254−1262.
(41) Wei, H.; Jenderka, M.; Bonholzer, M.; Grundmann, M.; Lorenz, M. Modeling the Conductivity around the Dimensionality-Controlled Metal-Insulator Transition in LaNiO3/LaAlO3 (100) Superlattices. *Appl. Phys. Lett.* **2015**, *106* (4), 042103.
(42) Mambrini, G. P.; Leite, E. R.; Escote, M. T.; Chiquito, A. J.; Longo, E.; Varela, J. A.; Jardim, R. F. Structural, Microstructural, and Transport Properties of Highly Oriented LaNiO3 Thin Films Deposited on SrTiO3 (100) Single Crystal. *J. Appl. Phys.* **2007**, *102* (4), 043708.
(43) Everhardt, A. S.; Dc, M.; Huang, X.; Sayed, S.; Gosavi, T. A.; Tang, Y.; Lin, C.-C.; Manipatruni, S.; Young, I. A.; Datta, S.; Wang, J.-P.; Ramesh, R. Tunable Charge to Spin Conversion in Strontium Iridate Thin Films. *Phys. Rev. Materials* **2019**, *3* (5), 051201.
(44) Rogado, N. S.; Li, J.; Sleight, A. W.; Subramanian, M. A. Magnetocapacitance and Magnetoresistance Near Room Temperature in a Ferromagnetic Semiconductor: La2NiMnO6. *Adv. Mater.* **2005**, *17* (18), 2225−2227.
(45) Guo, H.; Gupta, A.; Varela, M.; Pennycook, S.; Zhang, J. Local Valence and Magnetic Characteristics of La 2 NiMnO 6. *Phys. Rev. B* **2009**, *79* (17), 172402.
(46) Kitamura, M.; Ohkubo, I.; Kubota, M.; Matsumoto, Y.; Koinuma, H.; Oshima, M. Ferromagnetic Properties of Epitaxial La2NiMnO6 Thin Films Grown by Pulsed Laser Deposition. *Appl. Phys. Lett.* **2009**, *94* (13), 132506.

https://doi.org/10.1021/acs.nanolett.3c03658
Nano Lett. 2024, 24, 1122−1129